10.2514/6.2014-2124

AIAA AVIATION Forum
16-20 June 2014, Atlanta, GA
11th AIAA/ASME Joint Thermophysics and Heat Transfer Conference

Simulation of Ablating Hypersonic Vehicles with Finite-Rate Surface Chemistry

Erin Farbar,* Hicham Alkandry, † Jonathan Wiebenga, ‡ and Iain D. Boyd §

Department of Aerospace Engineering, University of Michigan, Ann Arbor, Michigan, USA

For the purpose of predicting the environment encountered by hypersonic, ablating vehicles employing non-charring thermal protection systems, the coupling of a Navier-Stokes solver to both a material response code and finite-rate surface chemistry code is described. The Navier-Stokes solver used in this study is LeMANS, a three-dimensional computational fluid dynamics code used to simulate hypersonic flow fields including gas-phase nonequilibrium thermochemistry. The material response solver used in this study is MOPAR, an implementation of the one-dimensional control-volume finite-element method for modeling heat conduction and pyrolysis gas behavior. The finite-rate surface chemistry code used in this study is a generalized framework that allows for any number of several types of surface reactions, such as adsorption/desorption, Eley-Rideal recombination, Langmuir-Hinshelwood recombination, oxidation/reduction, and sublimation/condensation to be considered. The test case used in this study is the nosetip of the IRV-2 vehicle, which employed a thermal protection system composed of non-charring carbon. A detailed discussion is given of the strategies used to couple the flow field solver, the surface chemistry solver, and the material response solver. The results produced using two finite-rate surface chemistry models are compared to previous results produced using the assumption of chemical equilibrium at the surface of the vehicle for a number of trajectory points of the IRV-2 vehicle.

Nomenclature

A	parameter used to define Arrhenius rate coefficient
B'	ratio of the mass fraction of gaseous carbon to mass fraction of air at local surface conditions
C_{LH}	constant used to define a Langmuir-Hinshelwood reaction
D_k	diffusion coefficient of species k, m^2/s
e	specific energy of the material, J/kg
E	energy barrier for specified reaction type, J/mol
ϵ	emissivity of surface
γ_0	reaction efficiency
γ_{sub}	reaction efficiency for sublimation reaction
h	specific enthalpy of material, J/kg
h_w	specific enthalpy of gas-phase at wall, J/kg
$h_{b,w}$	specific enthalpy of bulk-phase at wall, J/kg
k_{fi}	forward rate coefficient for reaction i, units are reaction dependent
k_{bi}	backward rate coefficient for reaction i, units are reaction dependent
K	number of species considered in the surface system
$K_{c,i}$	concentration based equilibrium constant, units are reaction dependent
$K_{a,i}$	activity based equilibrium constant
κ_{tr}	conductivity of the translational-rotational energy mode, W/m/K
κ_{ve}	conductivity of the vibrational-electronic energy mode, W/m/K

*Research Investigator, Member AIAA. Email: efarbar@umich.edu
†Research Associate, Member AIAA.
‡Graduate Student, AIAA Student Member.
§James E. Knott Professor of Engineering, Fellow AIAA.

$\dot{m}_b$	total mass loss rate of bulk species due to surface reactions, kg/m^2/s
M_k	molar weight of species k, kg/mol
N	number of CFD iterations between MOPAR calls
N_b	number of bulk phases in simulation
N_s	number of gas-phase species in simulation
N_{nb}	number of species in bulk phase nb
N_R	number of surface reactions
n	wall normal coordinate (positive in direction normal to wall)
nb	bulk phase index
ν'_{ki}	stoichiometric coefficient of species k in reaction i on reactant side
ν''_{ki}	stoichiometric coefficient of species k in reaction i on product side
p_w	pressure at the wall, Pa
p_n	pressure at first cell next to the wall, Pa
ϕ_s	active site density, moles/m^2
$\mathbf{q}$	heat flux vector, W/m^2
q_{rad}	radiative heat flux absorbed by surface, W/m^2
q_{cond}	heat flux conducted from surface in solid, W/m^2
q_{conv}	convective heat flux, W/m^2
$\dot{Q}$	material response source term, W/m^3
R_w	recession of cell surface face, m
ρ_b	density of bulk phase, kg/m^3
ρ_n	gas-phase density at first cell next to the wall, kg/m^3
ρ_w	gas-phase density at wall, kg/m^3
$\dot{s}$	recession rate, m/s
S_0	sticking coefficient
σ	Stefan-Boltzmann constant, 5.670×10^{-8}W/m^2/K^4
T_a	activation temperature for chemical reactions, K
T_c	controlling temperature for chemical reactions, K
T_w	temperature at the wall, K
T_∞	freestream temperature, K
T_{tr}	temperature of translational-rotational mode, K
T_{ve}	temperature of vibrational-electronic mode, K
θ	damping parameter
ν	desorption attempt frequency, 1/s
$\mathbf{v_{cs}}$	velocity vector associated with recessing material surface, m/s
$\bar{v}_A$	thermal speed of participating molecule in gas phase, m/s
$\bar{v}_{2D,A}$	thermal speed of surface species in Langmuir-Hinshelwood reaction, m/s
v_w	wall normal velocity, m/s
v_n	velocity at first cell next to the wall, m/s
$\dot{w}_k$	molar production rate of species k, mol/m^2/s
X_k	concentration of species k, mol/m^3
Y_k	mass fraction of species k
$Y_{k,w}$	mass fraction of species k at wall

I. Introduction

Hypersonic vehicles can be required to sustain very high heat fluxes during flight through an atmosphere, and many such vehicles employ ablative Thermal Protection System (TPS) materials. In order to predict the surface properties of the vehicle and the radiative properties of the flow in the wake, models for complicated physical processes occurring on and in the material of the TPS, such as nonequilibrium surface chemistry, nonequilibrium pyrolysis chemistry, spallation, and charring, in addition to the models for nonequilibrium thermochemistry required in the gas-phase, are needed. This in turn requires methods of coupling the flow field solver to surface mass, momentum and energy boundary conditions. Inputs for the surface boundary conditions can be obtained from analytical models, or detailed surface chemistry and material response

models.

The primary purpose of this work is to develop a well-characterized coupling interface between an existing Finite Rate Surface Chemistry (FRSC) Module,[1–3] the LeMANS CFD code developed at the University of Michigan,[4–6] and the material response code MOPAR.[7] This will enable coupled flow field solutions to be generated that include the effects of nonequilibrium surface chemistry, potentially involving carbon oxidation, carbon nitridation, and surface catalysis, as well as the thermal response of the TPS material. The inputs to the FRSC Module are a set of chemical reaction mechanisms involving bulk, surface and gas-phase species, and the associated rates of those reactions. The main goal of this paper is to describe, in detail, the process for coupling the LeMANS CFD code to the FRSC module and the MOPAR material response code, and to present the difficulties encountered during the coupling process.

The second goal of this work is to illustrate the effect that the choice of surface chemical reaction model has on the predicted surface properties. To do this, surface temperature, convective heat flux, and mass ablation rates predicted using a finite-rate surface chemistry model are compared to predictions from previously reported results that were obtained using the assumption of chemical equilibrium at the surface of the vehicle through the use of B' tables.[8] Additionally, the sensitivity of the surface properties to the choice of chemical reaction mechanisms that are included in the finite-rate surface chemistry model is discussed.

The discussion in this paper focuses on non-charring thermal protection system (TPS) materials. In this case, ablation occurs solely through carbon removal by chemical reactions occurring at the surface. Mechanical ablation processes are not considered in this work. Models of varying complexity for the material response and surface chemistry components of the coupled computational framework have been applied to model the ablation of non-charring TPS materials. These approaches differ in how the chemical reactions at the surface are treated, how the response of the material to the aerothermal environment is modeled, and how the coupling between the CFD code and these components is accomplished. At perhaps the highest level of fidelity, the response of the material is modeled explicitly by solving the energy conservation equation, the chemical reactions at the surface are modeled using finite-rate mechanisms, and the flow field solution is tightly coupled to the material response model so that the boundary conditions are updated at each CFD iteration. This is the approach taken by Gosse et al.[9] Simplifications of the material response model include making the assumption of steady-state ablation, or the use of a measured surface temperature profile,[10] eliminating the need for a solution of the energy equation in the material. Many studies have utilized an assumption of a saturated equilibrium state between the surface and the gas to determine the composition at the surface and the mass flux of carbon due to ablation. This eliminates the need for a finite-rate surface chemistry model. Originally, the so-called B' tables were used, along with the heat-mass transfer analogy, to implement this type of boundary condition.[7,8,11,12] More recently, dedicated equilibrium chemistry routines have been coupled directly to the CFD code to eliminate the need for the heat-mass transfer analogy.[13,14] A recent assessment of the limitations of the application of the heat-mass transfer analogy and of a completely uncoupled approach to ablation modeling for a charring TPS is given by Johnston et al.[15] A loosely coupled finite-rate surface chemistry and material modeling approach has also recently been used for the simulation of charring TPS materials.[16,17]

The paper is presented as follows. The second section describes the IRV-2 test case that is investigated in this work. The third section describes the numerical method used in this study, and details regarding the Navier-Stokes solver, the material response code, and the finite-rate surface chemistry module are presented. The chemistry models used in both the gas phase and the surface phase are presented in this section. The fourth section gives a detailed presentation of the approach used to couple the Navier-Stokes solver to the material response code and the finite-rate surface chemistry module. In the fifth section of this paper, the flow field and surface properties predicted using each surface chemistry model are presented and compared. Additionally, the predicted properties at the stagnation point are compared to previously published results, and challenges encountered during the solution process are discussed. The last section of the paper presents the conclusions drawn from the study and possible future work directions.

II. Test Case: IRV-2

Simulations of the well-documented reentry trajectory of the IRV-2 vehicle are performed.[8,18] An image of the IRV-2 vehicle is shown in Figure 1(a). The IRV-2 vehicle is spherical biconic with a nose radius of 0.01905 m and a total length of 1.386 m. The biconic angles are 8.42 and 6.10 degrees, and the change in biconic angle occurs at an axial location of 0.1488 m, measured from the stagnation point. Only the first

cone is considered in this study.

The trajectory of the IRV-2 vehicle, including the modifications described in Ref. 8, is shown in Figure 1(b). The flight conditions that are simulated in this study correspond to the first seven points of the trajectory and are listed in Table 1. At the first trajectory point, the surface of the vehicle is assumed to be isothermal and at the same temperature as the freestream flow. The mesh used to obtain axisymmetric solutions of the flow around the forebody of the vehicle contains 96 cells in the axial direction and 88 cells along the body. The mesh provides grid independent solutions at the first trajectory point. The grid is moved with the recessing surface in this study, however the mesh is not adapted to the flow field at each trajectory point. The error associated with this simplification is expected to be small at the higher altitude trajectory points, but it is expected to increase as the ablation rate, and therefore the vehicle deformation, increases at the lower altitude trajectory points.

Table 1: Freestream conditions for the IRV-2 simulations.[8]

Trajectory point	Time [s]	Altitude [m]	Velocity [m/s]	Density [kg/m^3]	Temperature [K]
1	0.00	66940	6781	1.251×10^{-4}	227.8
2	4.25	55840	6788	5.045×10^{-4}	258.0
3	6.75	49290	6785	1.134×10^{-3}	270.7
4	8.75	44040	6773	2.259×10^{-3}	261.4
5	10.25	40110	6752	3.996×10^{-3}	250.5
6	11.50	36840	6722	6.427×10^{-3}	241.5
7	12.50	34230	6684	9.583×10^{-3}	234.3

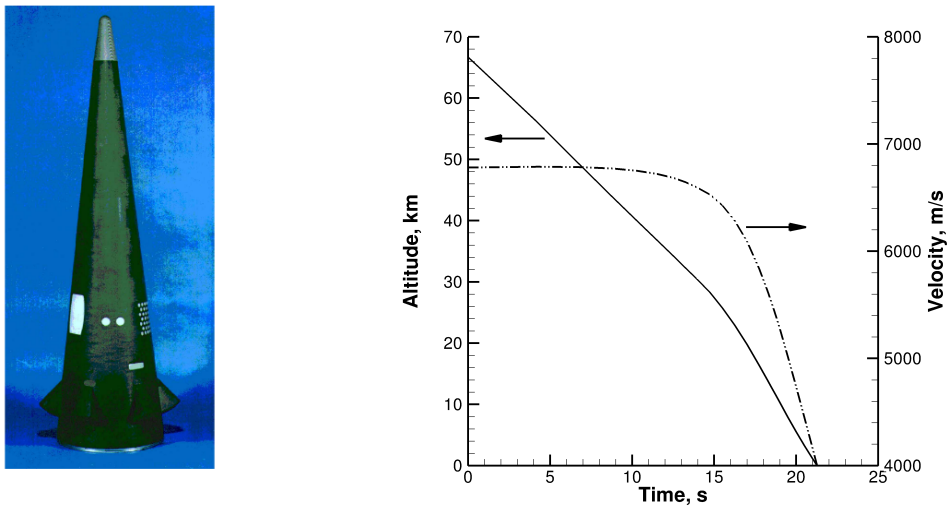

(a) IRV-2 vehicle (b) Trajectory

Figure 1: IRV-2 vehicle and re-entry trajectory.

III. Numerical method

III.A. Flow field

The properties of the nonequilibrium gas flow are obtained by solving the Navier-Stokes equations using a CFD code called LeMANS, which is developed at the University of Michigan.[5,6] LeMANS is a three-

dimensional, parallel code that solves the Navier-Stokes equations on unstructured meshes. In this work, it is assumed that the translational and rotational energy modes can be described by a single temperature, and that the vibrational, electronic and electron translational energy modes are described by a different temperature. The mixture transport properties are calculated using Wilke's semi-empirical mixing rule.[19] The species viscosities are calculated using Blottner's model[20] and the species thermal conductivities are calculated using Eucken's relation.[21] In this study, the Lewis number is constant with a value of 1.4. The mass diffusion fluxes are modeled using a modified version of Fick's law,[22] which enforces the requirement that the fluxes sum to zero, and the diffusion flux of electrons is calculated assuming ambipolar diffusion.

A second order spatially accurate finite-volume method is used to solve the set of partial differential equations on unstructured meshes. LeMANS can simulate two dimensional and axisymmetric flows using any mixture of quadrilateral and triangular mesh cells, and three-dimensional flows using any mixture of hexahedra, prisms, tetrahedra and pyramids. The inviscid fluxes are discretized using a modified Steger-Warming Flux Vector Splitting approach which has low dissipation and is appropriate to calculate boundary layers.[23] The viscous fluxes are calculated using cell-centered and nodal values. The viscous stresses are modeled assuming a Newtonian fluid and Stokes' hypothesis, and the heat fluxes are calculated according to Fourier's Law for all temperatures. A point or line implicit method is used to perform the time integration, and the code is parallelized using Metis[24] to partition the mesh, and the Message Passing Interface (MPI) to communicate information between processors.

In order to use LeMANS in coupled flow-material simulations, mesh movement capabilities have been implemented to model surface recession of ablating materials. Given the displacement of each node on the surface of the material, each node on the associated perpendicular line extending from the surface to the inflow boundary is moved along the line a distance proportional to the initial distance of the node in question from the surface node. This method of moving the mesh exploits the relatively simple, convex shape of hypersonic flight vehicles. Once the new mesh is created, the flow field quantities from the previous iteration are simply moved to the new mesh.

The chemistry model is adapted from Ref. 25, and consists of the following twenty species:

$$\mathrm{N_2,\ O_2,\ NO,\ N,\ O,\ N_2^+,\ O_2^+,\ NO^+,N^+,\ O^+,\ e}$$

$$\mathrm{CO,\ CO_2,\ C_3,\ CN,\ C,\ C_2,\ NCO,\ CO^+,\ C^+}$$

The forward reaction rates are specified in Arrhenius format, $k_f = AT_c^{\eta} e^{-\frac{T_a}{T_c}}$, and they are listed in Table 2, which is adapted from Ref. 25. Park's two-temperature model[26] is used to set the controlling temperature for each reaction in order to account for the effect of thermal nonequilibrium on the reaction rates.

Table 2: Reactions considered for the chemistry model.

#	Reaction	A [mol,cm,s]	η	T_a [K]
1	$N_2 + M \rightleftharpoons N + N + M$	7.00×10^{21}	-1.6	113200.0
		N, N^+ enhanced by 4.28		
		O, O^+ enhanced by 4.28		
		C, C^+ enhanced by 4.28		
		e enhanced by 1000		
2	$O_2 + M \rightleftharpoons O + O + M$	2.00×10^{21}	-1.5	59500.0
		N, N^+ enhanced by 5.00		
		O, O^+ enhanced by 5.00		
		C, C^+ enhanced by 5.00		
3	$NO + M \rightleftharpoons N + O + M$	5.00×10^{15}	0.0	75500.0
		N, N^+ enhanced by 20.0		
		O, O^+ enhanced by 20.0		
		C, C^+ enhanced by 20.0		
4	$CO + M \rightleftharpoons O + C + M$	2.30×10^{19}	-1.0	129000.0
		N, N^+ enhanced by 1.50		
		O, O^+ enhanced by 1.50		
		C, C^+ enhanced by 1.50		
5	$NCO + M \rightleftharpoons N + CO + M$	6.30×10^{16}	-0.5	24000.0
6	$CO_2 + M \rightleftharpoons O + CO + M$	3.50×10^{14}	0.0	52525.0
7	$CN + M \rightleftharpoons C + N + M$	2.53×10^{14}	0.0	71000.0
8	$C_2 + M \rightleftharpoons 2C + M$	4.50×10^{18}	-1.0	70930.0

Continued on next page

Table 2 – continued from previous page

#	Reaction	A [mol,cm,s]	η	T_a [K]
9	$N_2 + O \rightleftharpoons N + NO$	6.40×10^{17}	-1.0	38370.0
10	$NO + O \rightleftharpoons N + O_2$	8.40×10^{12}	0.0	19450.0
11	$C + N_2 \rightleftharpoons CN + N$	5.24×10^{13}	0.0	22600.0
12	$C + NO \rightleftharpoons CN + O$	2.02×10^{14}	-0.3	0.0
13	$C + NO \rightleftharpoons CO + N$	2.29×10^{13}	0.0	0.0
14	$C + O_2 \rightleftharpoons O + CO$	5.80×10^{13}	0.0	576.0
15	$C_2 + C_2 \rightleftharpoons C_3 + C$	3.20×10^{14}	0.0	0.0
16	$C_2 + N_2 \rightleftharpoons CN + CN$	1.50×10^{13}	0.0	21000.0
17	$CN + C \rightleftharpoons C_2 + N$	5.00×10^{13}	0.0	13000.0
18	$CN + CO \rightleftharpoons C + NCO$	1.50×10^{16}	-0.5	65800.0
19	$CN + CO_2 \rightleftharpoons CO + NCO$	4.00×10^{14}	0.0	19200.0
20	$CN + NO \rightleftharpoons N + NCO$	2.00×10^{13}	0.0	21000.0
21	$CN + O \rightleftharpoons CO + N$	2.41×10^{14}	-0.2	0.0
22	$CN + O_2 \rightleftharpoons O + NCO$	1.05×10^{13}	0.0	0.0
23	$CO_2 + O \rightleftharpoons CO + O_2$	2.10×10^{13}	0.0	27800.0
24	$N + CO_2 \rightleftharpoons NO + CO$	3.00×10^{12}	0.0	5690.2
25	$NCO + N \rightleftharpoons N_2 + CO$	2.00×10^{13}	0.0	0.0
26	$NCO + NO \rightleftharpoons N_2 + CO_2$	3.80×10^{18}	-2.0	402.8
27	$NCO + O \rightleftharpoons NO + CO$	2.35×10^{13}	0.0	0.0
28	$NCO + O_2 \rightleftharpoons NO + CO_2$	2.00×10^{12}	0.00	10071.1
29	$N + e \rightleftharpoons N^+ + e + e$	2.5×10^{34}	-3.82	168600.0
30	$O + e \rightleftharpoons O^+ + e + e$	3.9×10^{33}	-3.78	158500.0
31	$C + e \rightleftharpoons C^+ + e + e$	3.7×10^{31}	-3.0	130720.0
32	$O + N \rightleftharpoons NO^+ + e$	5.30×10^{12}	0.0	31900.0
33	$O + O \rightleftharpoons {O_2}^+ + e$	1.1×10^{13}	0.00	80600.0
34	$N + N \rightleftharpoons {N_2}^+ + e$	2.0×10^{13}	0.00	67500.0
35	$C + O \rightleftharpoons CO^+ + e$	8.80×10^{8}	1.0	33100.0
36	$C + N \rightleftharpoons CN^+ + e$	1.00×10^{15}	1.50	164000.0
37	$N_2 + {O_2}^+ \rightleftharpoons {N_2}^+ + O_2$	9.9×10^{12}	0.00	40700.0
38	$N^+ + N_2 \rightleftharpoons {N_2}^+ + N$	1.0×10^{12}	0.50	12200.0
39	$CN^+ + N \rightleftharpoons CN + N^+$	9.80×10^{12}	0.0	40700.0
40	$CO + C^+ \rightleftharpoons CO^+ + C$	1.0×10^{13}	0.00	31400.0
41	$NO^+ + C \rightleftharpoons NO + C^+$	1.0×10^{13}	0.00	23200.0
42	$NO^+ + N \rightleftharpoons N_2^+ + O$	7.20×10^{13}	0.0	35500.0
43	$NO^+ + N \rightleftharpoons O^+ + N_2$	3.4×10^{13}	0.00	12800.0
44	$NO^+ + O \rightleftharpoons N^+ + O_2$	1.0×10^{12}	0.50	77200.0
45	$NO^+ + O \rightleftharpoons {O_2}^+ + N$	7.2×10^{12}	0.29	48600.0
46	$NO^+ + O_2 \rightleftharpoons {O_2}^+ + NO$	2.4×10^{13}	0.41	32600.0
47	$O^+ + NO \rightleftharpoons N^+ + O_2$	1.4×10^{5}	1.90	15300.0
48	$O^+ + N_2 \rightleftharpoons {N_2}^+ + O$	9.1×10^{11}	0.36	22800.0
49	$O_2^+ + N \rightleftharpoons N^+ + O_2$	8.70×10^{13}	0.1	28600.0
50	${O_2}^+ + O \rightleftharpoons O_2 + O^+$	4.0×10^{12}	-0.09	18000.0
51	$O_2 + C^+ \rightleftharpoons {O_2}^+ + C$	1.0×10^{13}	0.00	9400.0

III.B. Material response

In this work, a one-dimensional (MOPAR) material response model is used. The MOPAR module uses the one-dimensional control volume finite-element method (CVFEM)[27,28] to model heat conduction and pyrolysis gas behaviour. Since a non-charring TPS material is investigated in this study, only the heat conduction modeling capability is used here. Details of the MOPAR module as well as the results of validation studies can be found in Refs. 7 and 29.

MOPAR is used to solve the energy equation in the material, which is shown in Equation 1. This equation includes a convection term due to grid motion to allow for the material mesh to recede when surface ablation is occurring,

$$\rho \frac{\partial e}{\partial t} - \rho h (\nabla \cdot \mathbf{v_{cs}}) + \nabla \cdot \mathbf{q} = \dot{Q} \tag{1}$$

Equation 1 is solved implicitly in MOPAR. The Backward Euler method is used for implicit time integration, which leads to a first order accurate discretization in time. The control surface velocity is determined from

the change in node positions during a time step as the mesh is deformed.

For the simulations discussed in this work, the material properties of the bulk carbon TPS are set to those of generic non-charring carbon.[27] The length of the solid computational domain is 0.01905 m and consists of 101 grid points along each surface line. A zero-gradient boundary condition is enforced at the end of each line, and the boundary condition at the surface is set as described in Section IV.B.

III.C. Finite-rate surface chemistry

The FRSC module developed by Marschall and MacLean[2,3] is tightly coupled to the LeMANS CFD code. The FRSC module allows the specification of surface reactions involving both adsorbed surface species and bulk material species. These reactions are governed by sets of active sites, and by types of bulk species. Given the conditions at the vehicle surface from the CFD code, the module computes the species production rates due to surface reactions. These values are then communicated to the CFD code. The module also has the capability to model the blowing of pyrolysis gases from the surface, however this capability is not used in the present work because the behaviour of a non-charring carbon ablator is investigated. The coupling of the FRSC module to the LeMANS CFD code has been verified.[30]

The FRSC Module allows for the definition of three distinct environments: gas, surface, and bulk. The surface and bulk environments can have any number of phases, which represent physically and chemically distinct regions. The gas environment can only have a single phase. Surface reactions may only occur at active sites that can either be empty or filled with an adsorbed species on a specific surface phase. The total number of reaction sites is conserved and sites may neither be created nor destroyed. The number of reaction sites (i.e. site density) is a property of the surface and is defined as a user input. The FRSC Module allows the specification of several different reaction types. These include,

Adsorption/Desorption:	$\mathrm{A} + (\mathrm{s}) \rightleftharpoons \mathrm{A(s)}$
Eley-Rideal:	$\mathrm{A} + \mathrm{B(s)} \rightleftharpoons \mathrm{AB} + (\mathrm{s})$
Langmuir-Hinshelwood:	$\mathrm{A(s)} + \mathrm{B(s)} \rightleftharpoons \mathrm{AB} + (\mathrm{s})$
Sublimation/Condensation:	$(\mathrm{s}) + \mathrm{A(b)} \rightleftharpoons \mathrm{A} + (\mathrm{s})$

In the previous examples, (s) represents an empty active site, A(s) is an adsorbed particle, and A(b) is a bulk species. The FRSC Module also allows for the specification of several other reaction processes that do not strictly fit into the categories given above (e.g. oxidation and nitridation).

The general form for reaction i can be expressed as,

$$\sum_{k=1}^{K} \nu'_{ki} A_k \rightleftharpoons \sum_{k=1}^{K} \nu''_{ki} A_k \tag{2}$$

The net production rate for species k from all N_R surface reactions is,

$$\dot{w}_k = \sum_{i}^{N_R} \dot{w}_{ki} \tag{3}$$

where the reaction-specific production rate is given by,

$$\dot{w}_{ki} = (\nu''_{ki} - \nu'_{ki}) \left(k_{fi} \prod_{k=1}^{K} X_k^{\nu'_{ki}} - k_{bi} \prod_{k=1}^{K} X_k^{\nu''_{ki}} \right) \tag{4}$$

The forward reaction rates for surface processes are specified using kinetics-based formulations for specific reaction types as,

Adsorption:

$$k_f = \left[\frac{\bar{v}_A}{4\phi_s^{\nu_s}} \right] S_0 \exp\left(-\frac{E_{ad}}{RuT} \right) \tag{5}$$

Eley-Rideal:

$$k_f = \left[\frac{\bar{v}_A}{4\phi_s^{\nu_s}} \right] \gamma_0 \exp\left(-\frac{E_{ER}}{RuT} \right) \tag{6}$$

Langmuir-Hinshelwood:

$$k_f = \left[\bar{v}_{2D,A}\sqrt{Av}\right] \phi_s^{1.5-\nu_s} C_{LH} \exp\left(-\frac{E_{LH}}{RuT}\right) \tag{7}$$

Sublimation:

$$k_f = \left[\frac{\bar{v}_A}{4\phi_s^{\nu_s} RuT}\right] \gamma_{sub} \exp\left(-\frac{E_{sub}}{RuT}\right) \tag{8}$$

In these equations, the parameters $E_{ad}, E_{ER}, E_{LH}, E_{sub}$ are the energy barriers for each type of reaction mechanism. The reaction efficiency, γ_0, is defined as the ratio of the flux of atoms at the surface that react to the total flux of atoms impinging on the surface. The sticking or adsorption coefficient, S_0, is the fraction of gas-phase species that hit the surface and become adsorbed. The molecular weight of species A is given by M_A, γ_{sub} is a dimensionless evaporation coefficient, and C_{LH} is a dimensionless constant. The total active site density of the surface phase where the reaction takes place is given by ϕ_s. Note that this parameter appears in Equation 4 for the production rate, and so the overall production rate is independent of the value chosen for this parameter, unless reactions are competing for active sites.

The thermal velocities used in the rate expressions are given by,

$$\bar{v}_A = \sqrt{\frac{8RuT}{\pi M_A}} \tag{9}$$

and

$$\bar{v}_{2D,A} = \sqrt{\frac{\pi RuT}{2M_A}} \tag{10}$$

$\bar{v_{2D,A}}$ is the thermal speed of surface species participating in a Langmuir-Hinshelwood reaction, and species A is then associated with the adsorbed surface species. In the case of Adsorption and Eley-Rideal reactions, $\bar{v_A}$ is the thermal speed of the participating molecule in the gas phase, and for sublimation reactions, $\bar{v_A}$ is the thermal speed of the sublimating species in the sublimation reaction. The temperature used in these expressions is the translational temperature of the gas at the surface, which is equal to the wall temperature for this work. This approach of defining the forward reaction rates is more insightful than using Arrhenius-type expressions since the Arrhenius reaction parameters may be difficult to relate to physical, chemical, or kinetic processes. Note, however, that the FRSC Module also allows for Arrhenius-type formulations for the forward rates.

The backward rate for reaction i is determined based on the forward rates and the concentration-based equilibrium constant by,

$$k_{b,i} = \frac{k_{f,i}}{K_{c,i}} \tag{11}$$

The concentration-based equilibrium constant is related to the activity-based equilibrium constant by,

$$K_{c,i} = K_{a,i} \left(\frac{P_{ref}}{RuT}\right)^{\nu_{g,i}} \tag{12}$$

where P_{ref} is a reference pressure of 10^5 Pa, which is the same value used in the NASA Glenn thermodynamic database,[31] and $\nu_{g,i}$ is the net stoichiometric exponent for gas species equal to $\sum(\nu''_{ki} - \nu'_{ki})$. The activity-based equilibrium constant is related to changes in the Gibbs energy of formation and can be calculated directly if the necessary thermodynamic properties are available by,

$$K_{a,i} = \exp\left[-\frac{\Delta G_i^0(T)}{RuT}\right] \tag{13}$$

where the change in Gibbs energy of formation, $\Delta G_i^0(T)$, can be obtained from databases, such as the NASA Glenn thermodynamic database.[31] However, the difference between the Gibbs energy of formation of an occupied active site and an empty active site may not be available for most species. For these cases, either the backward rate $k_{b,i}$ or the concentration-based equilibrium constant $K_{c,i}$ must be specified in addition to the forward rate for each adsorption reaction based on statistical thermodynamics and/or kinetic theory. Then, the missing thermodynamic data for occupied and empty active sites can be calculated using

Equations 12 and 13. The calculated change in Gibbs energy of formation can then be used with the available thermodynamic data for gas and solid phase species to calculate the constants for all other surface reactions. Additional details regarding the FRSC Module are provided in Ref. 2.

The finite-rate surface chemistry model used to generate baseline results for the IRV-2 vehicle is the Park model.[32,33] The surface reaction mechanisms considered in the Park model are listed in Table 3, along with the parameters used to model those reactions with the FRSC Module, which were taken from Ref. 3. Park's model includes irreversible oxidation of bulk carbon by atomic oxygen and molecular oxygen, as well as irreversible carbon nitridation and reversible carbon sublimation reactions.

Table 3: Original Park surface chemistry model.

Number	Reaction mechanism	Reaction type	Parameter	E [kJ/mol]
1	$O + (s) + C(b) \rightarrow CO + (s)$	Eley-Rideal	$\gamma_0 = 0.63$	9.644
2	$O_2 + 2(s) + 2C(b) \rightarrow 2CO + 2(s)$	Eley-Rideal	$\gamma_0 = 0.50$	0
3	$N + (s) + C(b) \rightarrow CN + (s)$	Eley-Rideal	$\gamma_0 = 0.30$	0
4	$3(s) + 3C(b) \rightarrow C_3 + 3(s)$	sublimation	$\gamma_{sub} = 5.19\times10^{13}$	775.81
5	$C_3 + 3(s) \rightarrow 3(s) + 3C(b)$	Eley-Rideal	$\gamma_0 = 0.10$	0

The use of the Park model to predict recession rates in arc-jet tests of Phenolic Impregnated Carbon Ablator (PICA) has indicated that the reaction efficiency for the carbon nitridation reaction is likely too high, and replacement of the carbon nitridation reaction with reactions modeling the recombination of nitrogen has produced better agreement with experimental data.[34] This modification leads to the second surface chemistry model that is investigated, shown in Table 4, which is referred to as the modified Park model.

Table 4: Modified Park surface chemistry model.

Number	Reaction mechanism	Reaction type	Parameter	E [kJ/mol]
1	$O + (s) + C(b) \rightarrow CO + (s)$	Eley-Rideal	$\gamma_0 = 0.63$	9.644
2	$O_2 + 2(s) + 2C(b) \rightarrow 2CO + 2(s)$	Eley-Rideal	$\gamma_0 = 0.50$	0
3	$N + (s) \rightarrow N(s)$	Adsorption	$\gamma_0 = 0.05$	0
4	$N + N(s) \rightarrow N_2 + (s)$	Eley-Rideal	$\gamma_0 = 0.05$	0
5	$3(s) + 3C(b) \rightarrow C_3 + 3(s)$	sublimation	$\gamma_{sub} = 5.19\times10^{13}$	775.81
6	$C_3 + 3(s) \rightarrow 3(s) + 3C(b)$	Eley-Rideal	$\gamma_0 = 0.10$	0

IV. Coupling Approach

IV.A. Implementation of Finite-Rate Surface Chemistry Coupling

The FRSC module is coupled to the CFD module through the mass balance and momentum balance equations written at the surface of the vehicle. The control volume enclosing the surface of the vehicle is drawn in Figure 2, where the terms appearing in the mass conservation equation are labeled. Using Figure 2, the mass conservation equation can be written at the surface for each species,

$$-\rho_w D_k \frac{\partial Y_k}{\partial n}|_w + \rho_w v_w Y_{k,w} = M_k \dot{w}_k \tag{14}$$

In Equation 14, the gas phase velocity is assumed to be in the surface-normal direction. Equation 14 is coupled to the expression for the mass flux of bulk species at the surface ($\dot{m}_b$) by the following relation,

$$\dot{m}_b = -\sum_{k=1}^{N_{nb}} M_k \dot{w}_k = \rho_w v_w \tag{15}$$

In Equation 15, the mass flux between the bulk and the gas environment due to surface reactions is computed by summing the mass production rates of N_{nb} bulk species. In an air-carbon system, this expression contains a single term for the production rate of solid carbon, $\dot{w_C}$, which will be negative if the surface is ablating (mass is being transfered from the bulk to the gas phase).

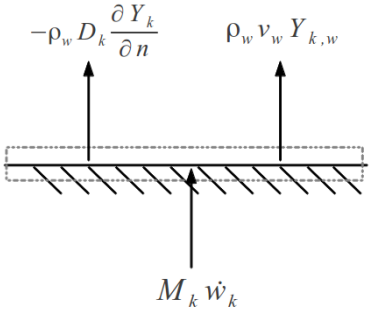

Figure 2: Control volume for species mass conservation at the surface of the vehicle.

The boundary conditions at the surface of the vehicle are determined at each iteration of the CFD solver as follows. The production rates of each gas, surface and bulk-phase species, $\dot{w}_k$, at the current iteration are calculated by the FRSC module using the values of ρ_w, $Y_{w,k}$ and T_w from the previous iteration. The production rates of the gas-phase species needed for the solution of Equation 14 are then known. The mass flux of the bulk-phase species, and thus the product $\rho_w v_w$, is then computed in LeMANS using the production rates of the bulk-phase species and Equation 15. The value of $\rho_w v_w$ is then substituted into Equation 14, and the system of N_s equations represented by Equation 14 is solved iteratively, together with the expression of momentum conservation at the surface (neglecting viscous terms),

$$p_n + \rho_n v_n^2 = p_w + \rho_w v_w^2 \tag{16}$$

using Newton's method in order to obtain the species mass fractions and gas-phase density required to set the boundary conditions at the wall. In Equation 16, the subscript "n" refers to a value in the first CFD cell lying along the material surface boundary, and "w" refers to a value at the surface face.

Since the system of equations is over-specified, the equation corresponding to the largest mass fraction is removed from the system prior to the solution process. The ideal gas law is used to eliminate the wall pressure, p_w, in Equation 16, and the temperature at the wall is known at the current iteration from the material response module. All of the primitive quantities at each cell-face that defines the surface of the vehicle are determined in this fashion at each iteration of the CFD solver, and the values of the conserved variables in the ghost cells are then calculated using these quantities in order to produce the required inviscid and viscous fluxes across the cell faces. Lastly, the concentrations of the surface species are updated at every iteration using a discrete form of Equation 17,

$$\frac{\partial X_k}{\partial t} = \dot{w}_k \tag{17}$$

where the time step used is the same simulation time step used in the CFD module.

The FRSC Module is designed to be coupled in a fully-implicit manner to the CFD code, however in this work, an explicit coupling scheme is used. As was described in detail above, this means that the values of the species mass fractions, density, and temperature from the previous iteration of the solver are used to calculate $\dot{w}_k$ and $\dot{m}_b$ in order to set the boundary conditions at the current iteration. A similar approach seems to have been adopted in Refs. 35 and 36.

IV.B. Implementation of Material Response Coupling

The MOPAR module is coupled to the LeMANS and the FRSC modules through the solution of the energy conservation equation at each cell face that defines the surface of the vehicle, as well as the calculated

recession rate of the vehicle's surface. The energy conservation equation at the surface of the vehicle is written using the control volume enclosing the surface of the vehicle that is shown in Figure 3:

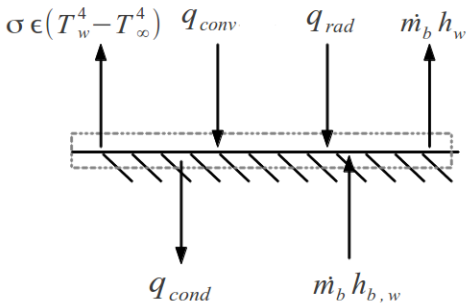

Figure 3: Control volume for energy conservation at the surface of the vehicle.

$$q_{conv} + \dot{m}_b h_{b,w} + q_{rad} = \sigma\epsilon\left(T_w^4 - T_\infty^4\right) + \dot{m}_b h_w + q_{cond}. \tag{18}$$

In Equation 18, the terms on the left-hand side represent energy entering the control volume shown in Figure 3, and the terms on the right-hand side represent energy leaving the control volume at the surface. The term labeled q_{conv} is the heat flux at the surface predicted by the CFD code,

$$q_{conv} = \kappa_{tr}\frac{\partial T_{tr}}{\partial n}|_w + \kappa_{ve}\frac{\partial T_{ve}}{\partial n}|_w + \sum_{k=1}^{N_s}\rho D_k h_k \frac{\partial Y_k}{\partial n}|_w, \tag{19}$$

and the term q_{cond} is the magnitude of the heat flux directed away from the surface and conducted into the solid that is predicted by the material response code. The radiative energy absorbed by the surface from the shock layer, q_{rad}, is neglected in this work. The energy radiated away from the surface, $\sigma\epsilon\left(T_w^4 - T_\infty^4\right)$, is computed in MOPAR. The recession rate at the surface of the vehicle is calculated in LeMANS as follows,

$$\dot{s}' = \frac{\dot{m}_b}{\rho_b}. \tag{20}$$

IV.C. Coupling Algorithm

The coupling between the CFD and FRSC modules and MOPAR proceeds as follows. The trajectory of the vehicle is discretized into several points. A steady state flow solution is then found at each trajectory point using the solution from the previous trajectory point as the initial condition. As the CFD-FRSC solution of the flow field is marched to steady state, the material response subroutine is called after every N flow field iterations, where N is a fixed number selected before running the simulation. The following input parameters are passed to MOPAR:

$$Q = \theta\left(q_{conv} + \dot{m}_b\left(h_{b,w} - h_w\right)\right) + (1-\theta)Q_{prev} \tag{21}$$

$$\dot{s} = \theta\dot{s}' + (1-\theta)\dot{s}_{prev} \tag{22}$$

In Equation 21, a subscript of "prev" is used to denote values of parameters from the previous call to MOPAR. The parameter θ is a damping factor that can have a value between 0 and 1.

MOPAR is then used to model the material response in a time-accurate fashion between the current trajectory point (at t^n) and the previous trajectory point (at t^{n-1}). During this process, the applied heat flux is linearly interpolated between the values obtained from the converged, coupled solution at the previous trajectory point, and those from the current state of the coupled solution. The recession rate is piece-wise constant between trajectory points. Once the surface temperature, T_w', corresponding to the current state of the CFD-FRSC solution is determined, it is also damped as follows:

$$T_w = \theta T_w' + (1-\theta)T_{w,prev} \tag{23}$$

The surface temperature is used in the FRSC module to determine the production rate of each species, and to set the boundary conditions for the conservation equations in the gas-phase for the next N iterations of the coupled CFD and FRSC modules.

The distance each surface face moves in the time between subsequent trajectory points is calculated as follows:

$$R_w = \dot{s}\left(t^n - t^{n-1}\right) \tag{24}$$

The displacement of each node on the surface is then formed as an average of adjacent face-centered values of R_w. The movement of every node on each line of the CFD mesh that extends from the surface is then determined as being proportional to the original distance of the node from the associated surface node. This coupling process is repeated until the flow field residuals have converged.

The entire coupling strategy is represented schematically in Figure 4. In Figure 4, the surface pressure, p_w, that is communicated between LeMANS and MOPAR is only used if a charring ablator is being modeled. Similarly, the mass flux of pyrolyzed gas, $\dot{m}_g$, and composition of pyrolyzed gas, Y_g, are only used if a charring ablator is being modeled. This case is not considered in this study.

The temperature of the gas at the surface is assumed to be equal to the temperature of the solid surface, and all internal energy modes of the gas-phase are assumed to be in equilibrium. The values of the damping parameter θ, and the coupling frequency N, are inputs to the coupling algorithm and need to be selected to optimize the computational efficiency of the simulation, while maintaining the stability of the coupled simulation.

V. Results and Discussion

V.A. Baseline results

The results in this section are obtained using the original Park chemistry model, as shown in Table 3. The coupling parameters are set to the following values: N = 200, $\theta = 0.5$. The calculations begin with a CFL number of 0.8, corresponding to a CFD time step of 3×10^{-9} s, which is gradually increased until the maximum CFD time step of 1×10^{-7} s is reached at iteration 2000. At this point, the time step is held constant for the remainder of each simulation. The simulation at each trajectory point requires approximately 6000 CFD iterations to converge the L_∞ and L_2 residuals of the continuity equation to machine precision.

Figure 5 shows contours of translational temperature in the flow field around the vehicle, the streamlines of the flow, and contours of the temperature in the solid structure. Figure 5(a) shows the results predicted at the first trajectory point with ablation, at 4.25 s during the entry. Figure 5(b) shows the results predicted at the last trajectory point investigated in this study, at 12.5 s during the entry. The shock moves closer to the surface of the vehicle at the later trajectory point. Additionally, the peak flow temperature reached in the shock layer decreases, as a larger fraction of the molecular O_2 and N_2 in the flow is dissociated at the lower altitude point, which removes energy from the flow. The nose region of the solid structure reaches the highest temperature, just over 3500 K at the 12.5 s trajectory point, and the temperature of this region increases with increasing time of flight, as the heat load on the vehicle increases. The counter-intuitive shape of the temperature contours in the vicinity of Z = 0.02 m is explained by the fact that the flow of energy in the solid is modeled in one-dimension in this study, and therefore energy is constrained to flow in the direction of the local surface normal.

The predicted surface properties at each trajectory point are examined next. Figures 6(a) and 6(b) show profiles of surface temperature and mass flux of ablating carbon predicted using the original Park chemistry model along the surface of the IRV-2 vehicle for each trajectory point considered in this study. Both the surface temperatures and ablating mass fluxes are significantly higher in the nose region of the vehicle than along the rest of the surface, because the aerothermal environment is the most extreme in this region. The surface temperature increases with increasing time of flight, as expected. The ablating mass flux increases with increasing time of flight until the 12.5 s trajectory point, where the predicted mass flux along the surface of the vehicle at axial locations greater than Z = 0.05 m decreases relative to the value predicted at the 11.5 s trajectory point. This occurs because the density of oxygen and nitrogen atoms decrease in this region relative to the values at the 11.5 s trajectory point, reducing the values of $\dot{w_{CO}}$ and $\dot{w_{CN}}$, and therefore reducing the ablating mass flux.

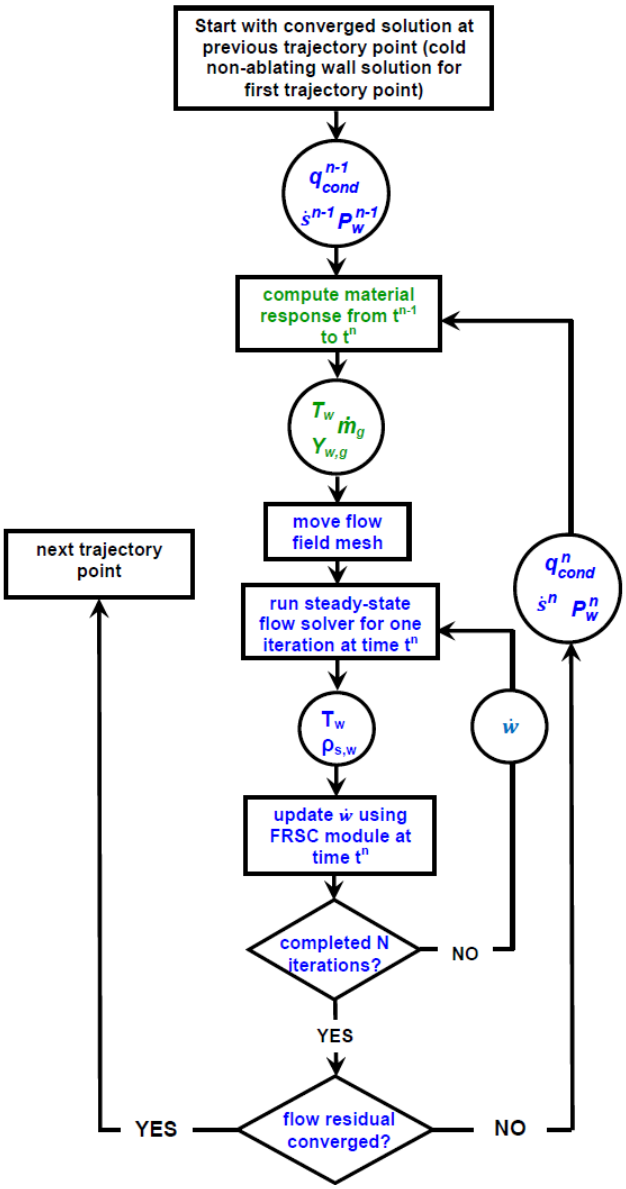

Figure 4: Coupling scheme between LeMANS-FRSC and MOPAR.

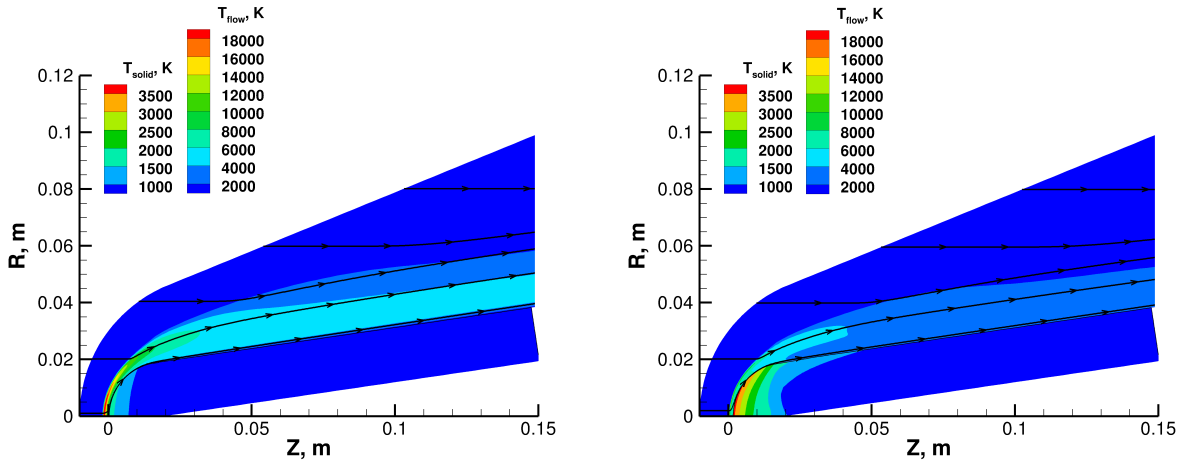

(a) 4.25 sec

(b) 12.5 sec

Figure 5: Contours of translational temperature, streamlines and temperature in the solid structure predicted using the original Park chemistry model at 4.25 s and 12.5 s.

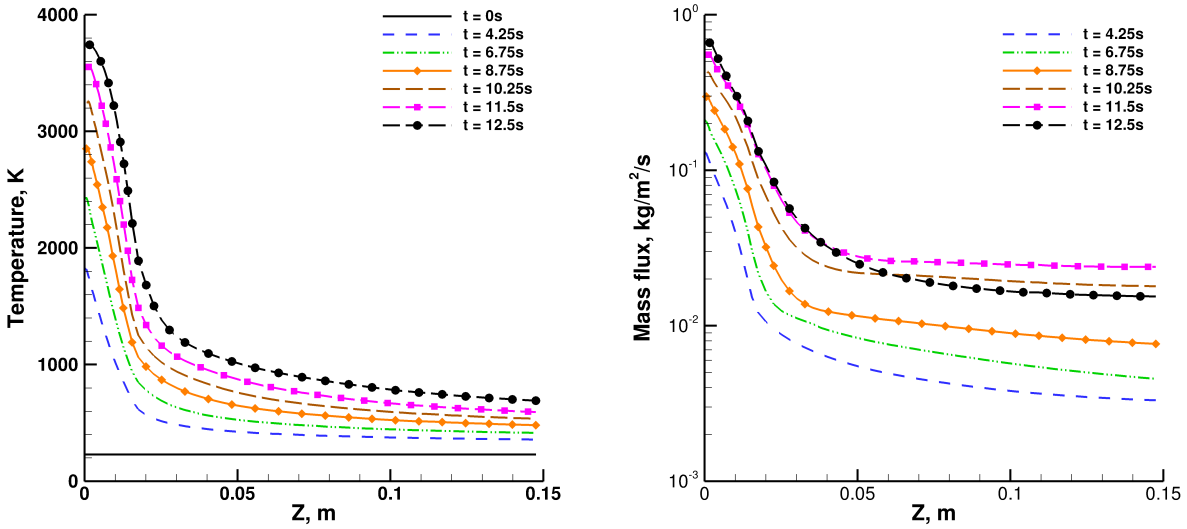

(a) Surface temperature

(b) Ablating mass flux

Figure 6: Predicted surface temperature and ablating mass flux using the original Park chemistry model along the length of the vehicle at each trajectory point.

The production rates due to chemical reactions along the surface are shown for the 4.25 s trajectory point in Figure 7(a) and for the 12.5 s trajectory point in Figure 7(b). The production rates predicted using the modified Park surface chemistry model are also shown on this Figure; these will be discussed in Section V.B. At the earlier trajectory point, C_3 is actually being consumed on the surface through Reaction 5 in Table 3. The production rates of CO and CN are of similar magnitude, and are much higher than the consumption rate of C_3. At the 12.5 s trajectory point, the production rates of both CN and C_3 have increased considerably, and C_3 is now being produced at the surface. Both the production of CN and C_3 peak at the stagnation point, where the temperature and overall density are the highest in the flow. However, the production rate of CO has approximately the same magnitude of that at the 4.25 s trajectory point, and peaks away from the stagnation point. This occurs because the density of oxygen atoms also peaks away from the stagnation point at the 12.5 s trajectory point.

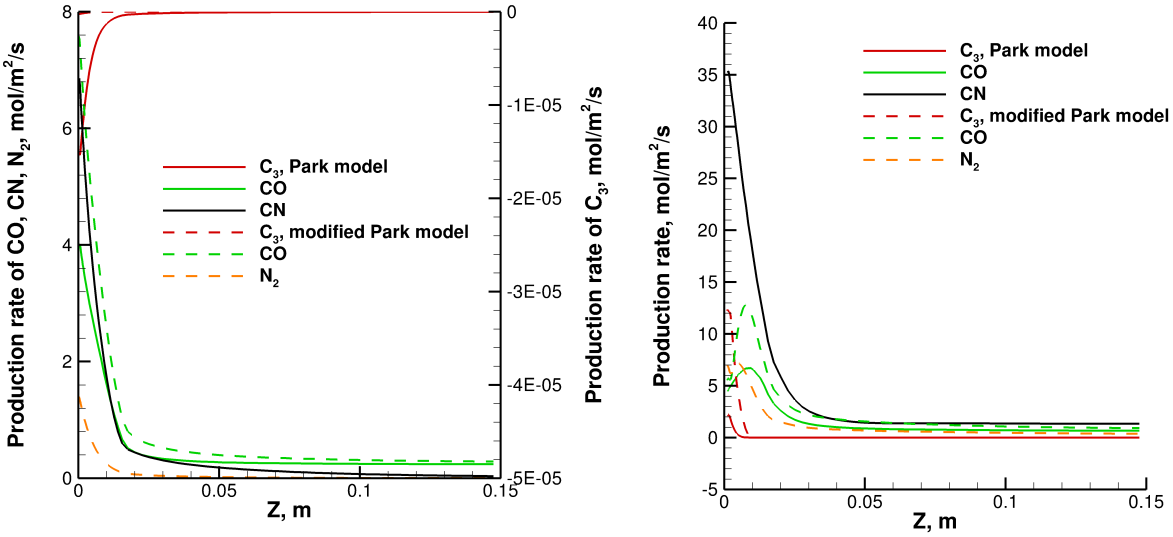

(a) 4.25 s

(b) 12.5 s

Figure 7: Productions rates of species created in surface chemical reactions along the length of the vehicle.

Profiles of each species along the stagnation streamline at the 12.5 s trajectory point are shown in Figure 8. Figure 8(a) shows the number density of neutral air species. As expected, the densities of both N_2 and O_2 rise sharply across the shock. The density of O_2 drops significantly immediately after the shock front, due to rapid dissociation to form O, and then drops again in the boundary layer close to the surface, due to consumption in the surface oxidation reaction. The density of N_2 increases in the boundary layer, because N atoms recombine to form N_2 in the high pressure boundary layer. The density of the products of dissociation reactions, N and O atoms, rise immediately after the shock, peak in the shock layer, and then drop in the boundary layer near the surface, because these atoms are consumed both in the oxidation and nitridation surface reactions, as well as in recombination reactions in the high density boundary layer.

Figure 8(b) shows the number density of carbon-containing species along the stagnation streamline. The dominant species are CO, C, and CN. Although Figure 7(b) shows that the production rate of CN is much larger than CO at the surface, the number density of CO is higher than that of CN throughout the shock layer. While the production rate determines the gradient of a species at the surface, the number density of a species is also a function of the production rates of that species in the bulk gas flow. CN is dissociated through Reaction 7 in Table 2 to form C and N, which may react with NO through Reaction 13, which has zero activation energy, to form CO. Additionally, Reaction 21 involves CN combining with O, which exists in abundance in the shock layer, to form CO. This reaction also has zero activation energy. Another possible reaction path for the consumption of CN is through Reaction 16, which involves two CN molecules combining to form C_2 and N_2. Some support for this is given by the fact that Figure 8(b) shows that C_2 is the fourth most abundant carbon-containing molecule near the wall, although C_2 is also formed via the consumption of

C_3 in Reaction 15. In fact, Reaction 15 is the only reaction in the gas-phase chemistry model that involves the consumption of C_3. Overall, these observations illustrate the fact that the gas-phase chemistry model plays an important role in determining the near-surface composition in the flow around a carbon ablator, a fact that has been demonstrated previously.[36]

Figure 8(c) shows the number density of charged species along the stagnation streamline. The most abundant ion is NO^+, which is formed in Reaction 32, the associative ionization with the lowest activation energy. The activation energies for the next two associative ionization reactions involving the creation of N_2^+ and O_2^+ are much higher, which explains the lower concentration of these ions. The N^+ and O^+ ions are created in the shock layer both through the direct ionization reactions, Reactions 29 and 30, and through charge exchange reactions, for example Reactions 43 and 44, both of which involve reactants that exist in the highest concentrations relative to the other species, namely, NO^+, N, and O. The densities of the two carbon-containing ions, CO^+ and C^+, peak near the surface and then drop rapidly through the shock layer. Due to the relatively high concentrations of C and O near the surface, the bulk of the CO^+ is likely created via the associative ionization reaction, Reaction 35. C^+ can be created by the direct ionization mechanism, Reaction 31, which has a large activation energy. It can also be created by various charge exchange reactions involving C, NO^+, CO^+, and O_2^+, all of which have much lower activation energies than the direct ionization reaction.

V.B. Comparison to the modified Park surface chemistry model

Results obtained using the modified Park chemistry model, shown in Table 4, are presented in this Section. Comparisons are made to the results obtained using the original Park chemistry model. The values of the coupling parameters and the CFD time step are the same as those used to obtain the results presented in the previous section for the simulations of the trajectory points two through five, however, the values had to be modified to obtain solutions for trajectory points six and seven. These modifications are discussed in Section V.C.

The predicted surface properties at each trajectory point are given in Figures 9(a) and 9(b), which show profiles of surface temperature and mass flux of ablating carbon predicted using the modified Park chemistry model along the surface of the IRV-2 vehicle for each trajectory point considered in this study. As was the case with the original Park chemistry model, both the surface temperatures and ablating mass fluxes are significantly higher in the nose region of the vehicle than along the rest of the surface, and the surface temperature increases with increasing time of flight, as expected. However, the ablating mass flux increases with increasing time of flight for all trajectory points when the modified Park chemistry model is used, in contrast to the behavior observed in Figure 6(b).

The convective heat flux, surface temperature, and ablative mass flux, predicted at the stagnation point using the modified Park model are compared to those predicted using the original Park model in Figure 10. Also shown on these Figures are the results of a previous numerical study that employed an equilibrium surface chemistry model in the form of the B' tables,[8] and the results predicted by the ABRES Shape Change Code (ASCC). ASCC is a correlation based code designed for predicting the performance of ablating nose-tips, has been shown to compare very well with flight data for ablating axisymmetric sphere-cones, and has flight data incorporated into its correlations.[8]

Figure 10(a) shows that the modified Park model predicts as much as a 25% higher heat flux than the original Park model until about 10 s into the trajectory, where the two surface chemistry models begin to predict similar heat flux values. Additionally, the results obtained using the modified Park model are in better agreement with the ASCC results. The heat flux predicted using the modified surface chemistry model at the 11.5 s trajectory point is slightly less than that predicted at the 10.25 s trajectory point. This is because as the time during the trajectory increases, the production rate of C_3 increases, an endothermic process with a heat of formation of 820 kJ/mol. Because the gradient of Y_{C_3} at the surface is negative, this results in a reduction in diffusive heat flux with increasing trajectory time, and this trend is predicted by both chemistry models. At the 11.5 s trajectory point, this reduction in diffusive heat flux predicted with the modified Park model is of a large enough magnitude to cause the overall convective heat flux to decrease slightly relative to the value at the 10.25 s trajectory point.

Figure 10(b) shows that the original Park chemistry model predicts a lower stagnation point temperature than the previously published results, while the modified Park chemistry models results in better agreement with the previously published values. Figure 10(c) shows that both the original Park chemistry model and the modified Park chemistry model predict a larger ablating mass flux at each trajectory point investigated

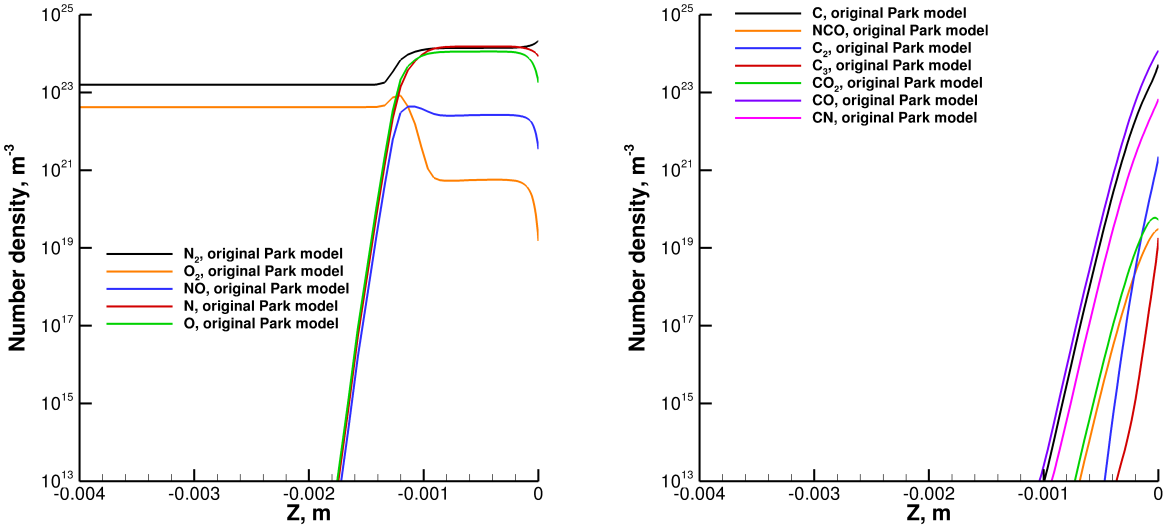

(a) Neutral species

(b) Carbon containing species

(c) Charged species

Figure 8: Predicted number density of each species along the stagnation streamline at 12.5 s using the original Park chemistry model.

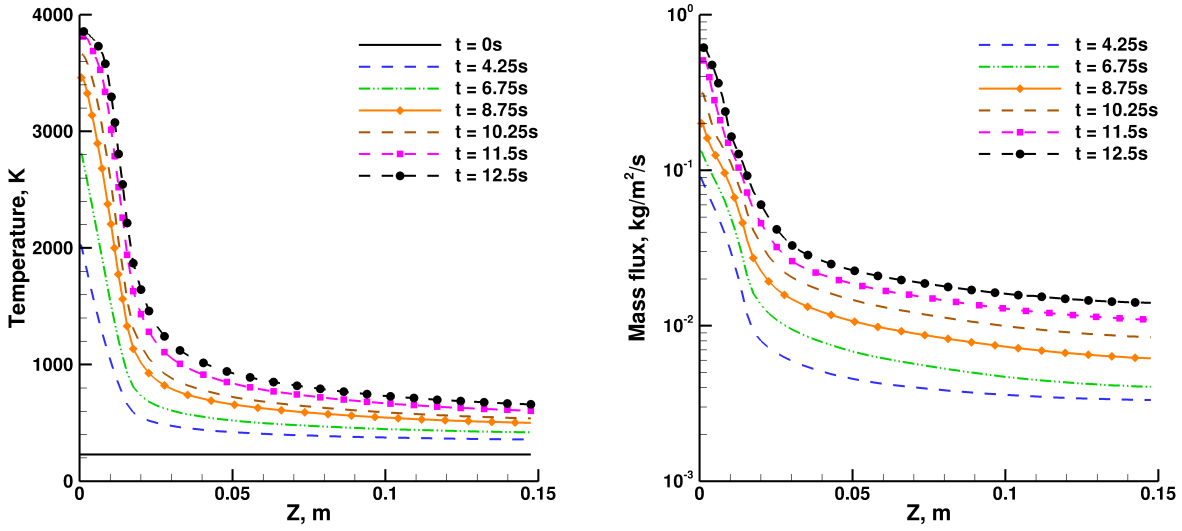

(a) Surface temperature

(b) Ablating mass flux

Figure 9: Predicted surface temperature and ablating mass flux using the modified Park chemistry model along the length of the vehicle at each trajectory point.

than the previously published results. However, the modified Park model predicts a lower ablating mass flux at each trajectory point than the original Park model, in better agreement with previously published results.

The production rates along the length of the vehicle predicted using the modified Park model are shown in Figure 7 for the first trajectory point with ablation, 4.25 s, and the last trajectory point considered in this study, 12.5 s. Note that when the original Park surface chemistry model is used, the production rate of N_2 is zero, as this reaction is not included in that model. Similarly, when the modified Park surface chemistry model is used, there is no production mechanism for CN, and the production rate of CN is therefore zero. At the 4.25 s trajectory point, the modified Park model predicts a much lower rate of consumption of C_3 than the original Park model does. This is because the surface temperature predicted by the modified Park model is higher than that predicted by the original Park model. The production rates of CO are similar between the two models, with the modified Park model predicting about twice the rate of production at the stagnation point relative to the original Park model. The production rate of CN in the original Park model is much higher than the production rate of N_2 in the modified Park model, which results in a decrease in the consumption of N at the surface when the modified model is used. This also results in a decrease in the predicted mass blowing rate at the surface relative to the original Park model, which is seen in Figure 10(c).

At the 12.5 s trajectory point, C_3 production has increased, and C_3 is being produced at a similar rate as CO. The modified Park model predicts a larger production rate of C_3, again because the predicted surface temperature is higher. The results obtained using the original Park model show that the CN production rate has increased dramatically relative to the value at the 4.25 s trajectory point, and the CN production rate is still much higher than the N_2 production rate predicted by the modified Park model. This is why the predicted mass ablation rate at the surface is also higher at this trajectory point when the original Park model is used, as shown in Figure 10(c). As was the case for the original Park model, the peak in the predicted CO production rate is downstream of the stagnation point at the 12.5 s flight condition.

The number densities of the carbon-containing species along the stagnation streamline predicted using each surface chemistry model at the 12.5 s trajectory point are shown in Figure 11. There is very little difference between the results predicted by the original and modified surface chemistry models; this observation is also true for the neutral species and charged species so those results are not shown here. Since both sets of simulations utilize the same gas-phase chemistry model, and very similar surface chemistry models, these similarities are not surprising. Figure 11 shows that there is a slight increase in the predicted densities of CO_2 and NCO near the surface, as well as a slight decrease in the predicted densities of C_2 and CN near

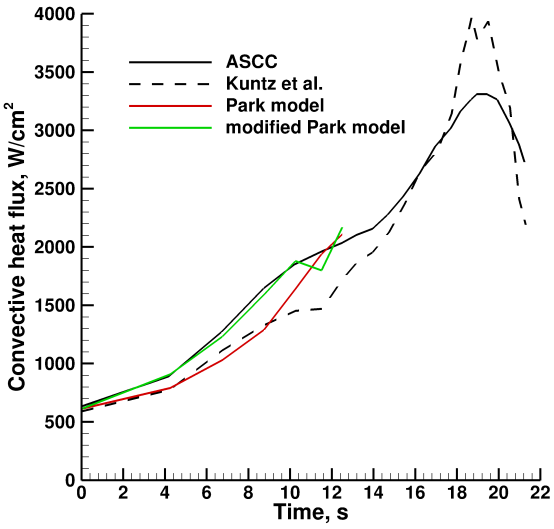

(a) Convective heat flux

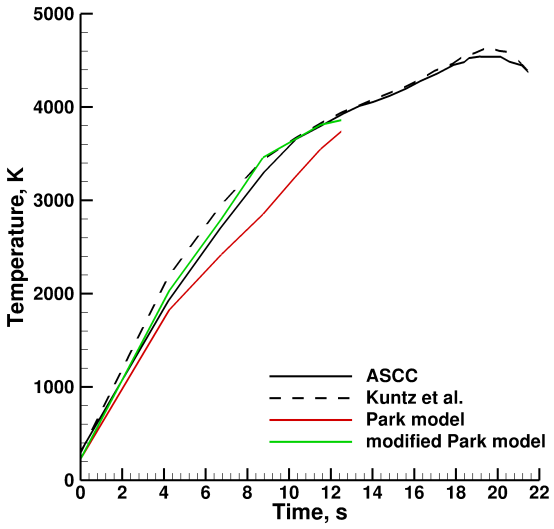

(b) Surface temperature

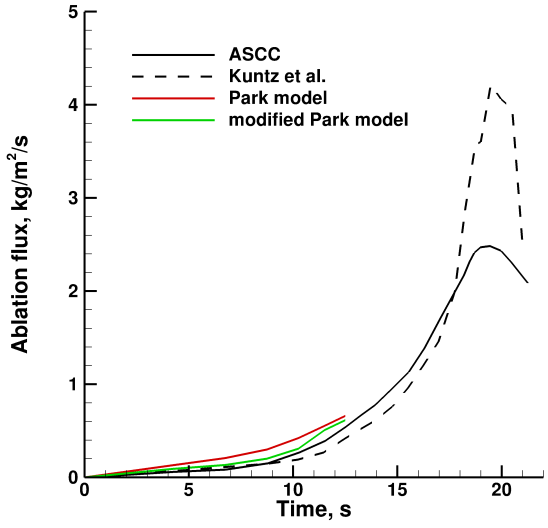

(c) Ablating mass flux

Figure 10: Convective heat flux, temperature and ablative mass flux predicted at the stagnation point.

the surface when the modified chemistry model is used. Lastly, the magnitude of the gradient in C_3 density near the surface is slightly larger when the modified chemistry model is used.

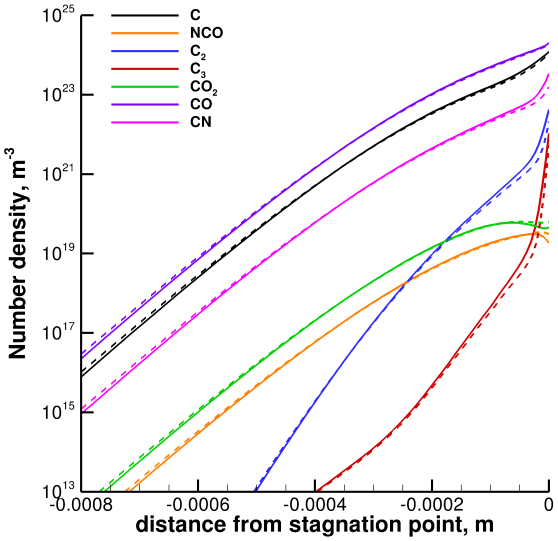

Figure 11: Predicted number density of carbon-containing species along the stagnation streamline at 12.5 s. Solid lines - original Park chemistry model. Dashed lines - modified Park chemistry model.

V.C. Coupling challenges

In the calculations of the 11.5 s trajectory point carried out using the modified Park chemistry model, the residual of the flow conservation equations enters a limit cycle, where the values do not decrease by more than two decades before MOPAR is called. This leads to the coupled simulation continuing for many more iterations than required to converge the simulations at the previous trajectory points, without achieving flow field convergence. To remedy this problem, the value of N is increased to 1000 iterations in order to obtain a fully converged solution at the 11.5 s trajectory point. Subsequently, a new method of determining when the surface temperature should be updated through a call to MOPAR is implemented. In this method, MOPAR is called only when the heat flux predicted at each cell face along the surface changes by less than a user-specified percentage between subsequent CFD iterations. Calls to MOPAR are ceased when the change in predicted surface heat flux at each cell face along the surface between subsequent calls to MOPAR is less than another user-specified percentage. The CFL ramp is reset after each call to MOPAR. In this work, the former value is set to 0.05%, and the latter is set to 1.0%.

Additionally, using the CFL ramp and coupling parameter θ described in Section V.A in the simulations of the 12.5 s trajectory point using the modified Park model leads to the calculation of negative surface mass fractions of O_2 and O in the nose-region of the vehicle surface, and ultimately to the simulation failing. The reason for this is explained by Figure 12, which shows the predicted temperature and production rate of O atoms at the stagnation point during both the original simulation with $\theta = 0.5$, as well as a new simulation in which a value of $\theta = 0.1$ is used, and the CFD time step is held at a constant value of $1{\times}10^{-8}$ s. The combination of these two modifications allow the new simulation to complete successfully. Figure 12(a) shows that the larger value of θ used in the original simulation leads to larger discontinuities in the temperature applied at the cell face located at the stagnation point. Figure 12(b) shows that these discontinuities in surface temperature result in discontinuities in the production rate of oxygen, with decreasing surface temperatures leading to increased production rates. This occurs because although the production rates are proportional to the square-root of surface temperature, they are also proportional to the density of reactant species at the surface, which is inversely proportional to the surface temperature. A very large decrease in surface temperature is predicted at approximately 4000 iterations in the simulation with $\theta = 0.5$, which results in a large increase in the production rate of CO, and therefore an increase in the consumption rate of O (it

becomes more negative). The required oxygen density gradient cannot be generated at the surface, and the predicted surface mass fraction of oxygen becomes negative. In Figure 12(b), the production rate of oxygen is actually oscillating after this event occurs, but the individual lines are not distinguishable on this Figure. This occurs because the surface mass fraction is set to a small value, in an attempt to allow the simulation to recover. It does not, and the simulation terminates at approximately 4200 iterations. In contrast, when a value of $\theta = 0.1$ is used, the temperature discontinuities and therefore production rate discontinuities are much smaller, and the simulation completes successfully.

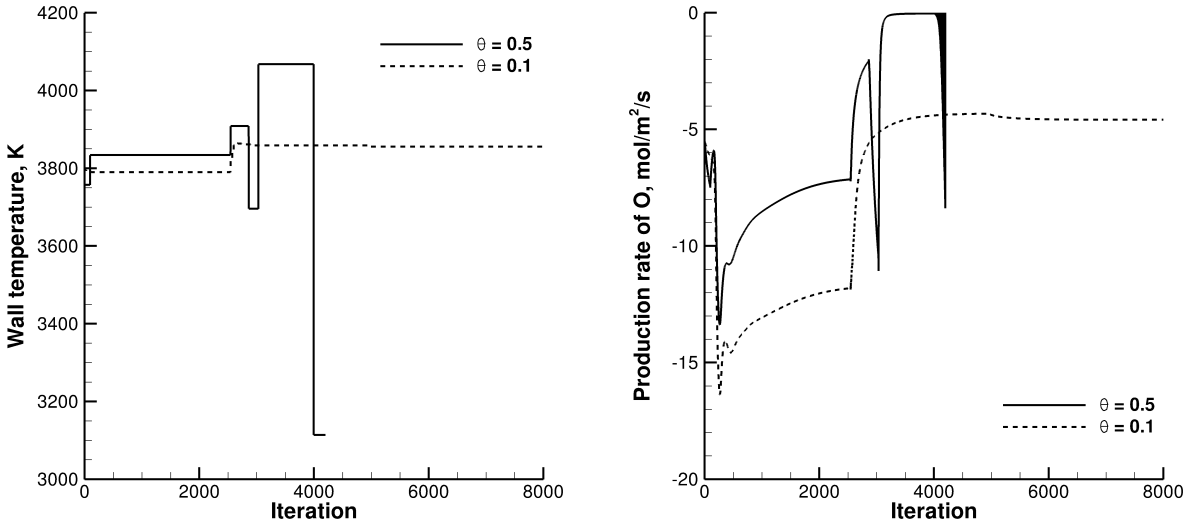

(a) Surface temperature

(b) Oxygen production rate

Figure 12: Surface temperature and oxygen production rate at the stagnation point during two instances of the simulation of the 12.5 s trajectory point using the modified Park surface chemistry model.

V.D. Sensitivity to choice of coupling parameters

An additional simulation of the first trajectory point with ablation, 4.25 s, is carried out to determine if the solutions generated by the coupling procedure described in Section IV are unique. Rather than calling MOPAR every N iterations, in this second simulation MOPAR is only called once the CFD result has converged. The parameter θ is set to a value of 1.0 in this additional simulation. Figure 13 shows the surface temperature along the surface of IRV-2 at the first ablating trajectory point, computed using both the baseline coupling procedure, and by converging the flow field before each MOPAR call. The lines indicating the baseline surface temperature result and the surface temperature predicted by converging the flow field before calling MOPAR are nearly coincident. The figure also shows the relative difference between the two temperature predictions. The results plotted in Figure 13 are produced after three calls to MOPAR with a converged flow field. The difference between the two temperature profiles is below 1% everywhere along the surface. The other surface properties and flow field properties show similar behaviour. This comparison suggests that the coupling procedure described in Section IV does produce solutions that are independent of the choice of the coupling parameters, N and θ.

VI. Conclusions and Future Work

A detailed description of a coupling interface between a CFD code, a finite-rate surface chemistry model and a material response code is presented. The coupled framework is used to produce solutions for the IRV-2 trajectory, and it is shown that the framework produces results for the predicted flow field and surface properties that are insensitive to the choice of coupling parameters.

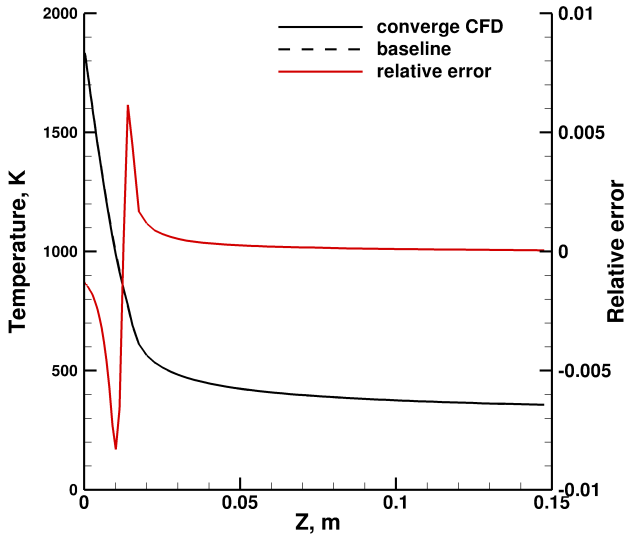

Figure 13: Surface temperature and relative error for IRV-2 at 4.25 s computed using two different coupling approaches.

The results presented here illustrate the effect that the choice of surface chemistry mechanisms and rates can have on the predicted surface properties. These effects are important because the predicted heat fluxes throughout the trajectory and the predicted heat load over the entire trajectory drive the sizing and material choices for a Thermal Protection System. As an example of the differences in the heat flux predictions produced by the two surface chemistry models discussed here, the modified Park model predicts a stagnation point heat flux at the 8.75 sec trajectory point that is approximately 25% higher than that predicted by the original Park model. This difference underscores the need for detailed studies of the air-carbon surface system, in order to increase the fidelity of the surface chemistry models required to perform simulations using this type of coupled computational framework.

The computational difficulties encountered at the 12.5 s trajectory point using the modified Park chemistry model indicate that more work on the robustness of the LeMANS-FRSC-MOPAR coupling interface may be needed in order to obtain coupled solutions at the later trajectory points of the IRV-2 trajectory.

Acknowledgments

The authors gratefully acknowledge the willingness of Matthew MacLean of CUBRC Inc. to share the Finite-Rate Surface Chemistry module that is used in this work. Additional thanks to Professor Alexandre Martin for his assistance with the MOPAR module. This work was funded by an MDA SBIR Phase II Contract.

References

[1]Marschall, J. and MacLean, M., *A Finite-Rate Surface Reaction Model for the Data-Parallel Line Relaxation (DPLR) Computational Fluid Dynamics Code*, SRI International and CUBRC, Inc., June.

[2]Marschall, J. and MacLean, M., "Finite-Rate Surface Chemistry Model, I: Formulation and Reaction System Examples," *AIAA-2011-3783*, presented at the 42nd AIAA Thermophysics Conference, Honolulu, Hawaii, June 2011.

[3]Marschall, J. and MacLean, M., "Finite-Rate Surface Chemistry Model, II: Coupling to Viscous Navier-Stokes Code," *AIAA-2011-3784*, presented at the 42nd AIAA Thermophysics Conference, Honolulu, Hawaii, June 2011.

[4]Scalabrin, L. C. and Boyd, I. D., "Numerical Simulation of Weakly Ionized Hypersonic Flow for Reentry Configurations," *AIAA Paper 2006-3773*, presented at the 9th AIAA/ASME Joint Thermophysics and Heat Transfer Conference, San Francisco, California, June 2006.

[5]Scalabrin, L. C., *Numerical Simulation of Weakly Ionized Hypersonic Flow Over Reentry Capsules*, Ph.D. thesis, The University of Michigan, 2007.

[6]Martin, A., Scalabrin, L. C., and Boyd, I. D., "High Performance Modeling of Atmospheric Re-entry Vehicles," *Journal of Physics: Conference Series*, Vol. 341, No. 1, 2012, Article 012002.

[7]Martin, A. and Boyd, I. D., "Strongly Coupled Computation of Material Response and Nonequilibrium Flow for Hypersonic Ablation," *AIAA-2009-3597*, presented at the 41st AIAA Thermophysics Conference, San Antonio, TX, June 2009.

[8]Kuntz, D. W., Hassan, B., and Potter, D. L., "Predictions of Ablating Hypersonic Vehicles Using an Iterative Coupled Fluid/Thermal Approach," *Journal of Thermophysics and Heat Transfer*, Vol. 15, No. 2, 2001, pp. 129–139.

[9]Gosse, R. and Candler, G. V., "Evaluation of Carbon-Carbon Ablation Models Using a Fully Coupled CFD Solver," *AIAA Paper 2008-3908*, presented at the 40th Thermophysics Conference, Seattle, Washington, June 2008.

[10]Chen, Y.-K. and Milos, F. S., "Navier-Stokes Solutions with Finite Rate Ablation for Planetary Mission Earth Reentries," *Journal of Spacecraft and Rockets*, Vol. 42, No. 6, 2005, pp. 961–970.

[11]Nompelis, I., Candler, G. V., and Conti, R. K., "A Parallel Implicit CFD Code for the Simulation of Ablating Re-Entry Vehicles," *AIAA-2009-1562*, presented at the 47th AIAA Aerospace Sciences Meeting and Exhibit, Orlando, Florida, Jan. 2009.

[12]Wiebenga, J. E. and Boyd, I. D., "Computation of Multi-dimensional Material Response Coupled to Hypersonic Flow," *AIAA-2012-2873*, presented at the 43rd AIAA Thermophysics Conference, New Orleans, Louisiana, June 2012.

[13]Gnoffo, P. A. and Johnston, C. O., "A Boundary Condition Relaxation Algorithm for Strongly Coupled, Ablating Flows Including Shape Change," *AIAA Paper 2011-3760*, presented at the 42nd AIAA Thermophysics Conference, Honolulu, Hawaii, June 2011.

[14]Bianchi, D., Nasuti, F., and Martelli, E., "NavierStokes Simulations of Hypersonic Flows with Coupled Graphite Ablation," *Journal of Spacecraft and Rockets*, Vol. 47, No. 4, 2010, pp. 554–562.

[15]Johnston, C. O., Gnoffo, P. A., and Mazaheri, A., "Study of Ablation-Flowfield Coupling Relevant to the Orion Heat Shield," *Journal of Thermophysics and Heat Transfer*, Vol. 26, No. 2, 2012, pp. 213–221.

[16]Alkandry, H., Boyd, I. D., and Martin, A., "Coupled Flow Field Simulations of Charring Ablators with Nonequilibrium Surface Chemistry," *AIAA Paper 2013-2634*, presented at the 44th Thermophysics Conference, San Diego, California, June 2013.

[17]Chen, Y.-K. and Gökçen, T., "Navier-Stokes Solutions with Finite Rate Ablation for Planetary Mission Earth Reentries," *Journal of Spacecraft and Rockets*, Vol. 42, No. 6, 2005, pp. 961–970.

[18]Thompson, R. A. and Gnoffo, P. A., "Implementation of a Blowing Boundary Condition in the LAURA Code," *AIAA Paper 2008-1243*, presented at the 46th AIAA Aerospace Sciences Meeting and Exhibit, Reno, Nevada, Jan. 2008.

[19]Wilke, C. R., "A Viscosity Equation for Gas Mixtures," *Journal of Chemical Physics*, Vol. 18, No. 4, 1950, pp. 517–519.

[20]Blottner, F. G., Johnson, M., and Ellis, M., "Chemically Reacting Viscous Flow Program for Multi-Component Gas Mixtures," Technical Report SC-RR-70-754, Sandia Laboratories, Albuquerque, New Mexico, 1971.

[21]Vincenti, W. G. and Kruger, C. H., *Introduction to Physical Gas Dynamics*, Krieger Publishing Company, 1965.

[22]Sutton, K. and Gnoffo, P. A., "Multi-Component Diffusion with Application to Computational Aerothermodynamics," *AIAA Paper 1998-2575*, presented at the 7th AIAA/ASME Joint Thermophysics and Heat Transfer Conference, Albuquerque, New Mexico, June 1998.

[23]MacCormack, R. W. and Candler, G. V., "The Solution of the Navier-Stokes Equations using Gauss-Seidel Line Relaxation," *Computers and Fluids*, Vol. 17, 1989, pp. 135–150.

[24]Karypis, G. and Kumar, V., "METIS: A Software Package for Partitioning Unstructured Graphs, Partitioning Meshes and Computing Fill-Reducing Orderings of Sparse Matrices," Tech. rep., University of Minnesota, 1998.

[25]Martin, A., Boyd, I. D., Cozmuta, I., and Wright, M. J., "Chemistry Model for Ablating Carbon-Phenolic Material During Atmospheric Re-entry," *AIAA-2010-1175*, presented at the 48th AIAA Aerospace Sciences Meeting and Exhibit, Orlando, Florida, Jan. 2010.

[26]Park, C., *Nonequilibrium Hypersonic Aerothermodynamics*, John Wiley and Sons, 1990.

[27]Amar, A. J., *Modeling of One-Dimensional Ablation with Porous Flow using Finite Control Volume Prodedure*, Master's thesis, North Carolina State University, Raleigh, NC, 2006.

[28]Blackwell, B. and Hogan, R., "Numerical Solution of Axisymmetric Heat Conduction Problems Using Finite Control Volume Technique," *Journal of Thermophysics and Heat Transfer*, Vol. 7, No. 3, 1993, pp. 462–471.

[29]Martin, A. and Boyd, I. D., "Simulation of Pyrolysis Gas within a Thermal Protection System," *AIAA-2008-3805*, presented at the 40th AIAA Thermophysics Conference, Seattle, Washington, June 2008.

[30]Alkandry, H., Farbar, E. D., and Boyd, I. D., "Evaluation of Finite-Rate Surface Chemistry Models for Simulation of the Stardust Reentry Capsule," *AIAA Paper 2012-2874*, presented at the 43rd AIAA Thermophysics Conference, New Orleans, Louisiana, June 2012.

[31]McBride, B. J., Zehe, M. J., and Gordon, S., "NASA Glenn Coefficients for Calculating Thermodynamic Properties of Individual Species," NASA/TP-2002-211556, National Aeronautics and Space Administration, September 2002.

[32]Park, C. and Ahn, H., "Stagnation-Point Heat Transfer Rates for Pioneer-Venus Probes," *Journal of Thermophysics and Heat Transfer*, Vol. 13, No. 1, 1999, pp. 33–41.

[33]Park, C., "Stagnation-Point Ablation of Carbonaceous Flat Disks - Part I: Theory," *AIAA Journal*, Vol. 21, No. 11, 1983, pp. 1588–1594.

[34]Driver, D. M. and MacLean, M., "Improved Predictions of PICA Recession in Arc Jet Shear Tests," *AIAA Paper 2011-0141*, presented at the 49th AIAA Aerosciences Meeting, Orlando, Florida, January 2011.

[35]Sorensen, C., Valentini, P., and Schwarztentruber, T. E., "Uncertainty Analysis of Reaction Rates in a Finite Rate Surface Catalysis Model," *AIAA Paper 2011-3643*, presented at the 42nd AIAA Thermophysics Conference, Honolulu, Hawaii, June 2011.

[36]Candler, G. V., "Nonequilibrium Processes in Hypervelocity Flows: An Analysis of Carbon Ablation Models," *AIAA-2012-0724*, presented at the 50th AIAA Aerospace Sciences Meeting, Nashville, Tennessee, January 2012.